AGU ADVANCING EARTH AND SPACE SCIENCES

Earth and Space Science

RESEARCH ARTICLE
10.1029/2025EA004201

Remote Sensing of Alpine Peatlands: Challenges of Mapping Thousands of Sparse Small Sites Scattered Across Extensive Mountainous Territories

Qiqi Li[1], **Manudeo Singh**[2,3], **and Sonia Silvestri**[1]

[1]Department of Biological, Geological, and Environmental Sciences, University of Bologna, Bologna, Italy, [2]Institute of Geosciences, University of Potsdam, Potsdam, Germany, [3]Now at Department of Geography and Earth Sciences, Aberystwyth University, Wales, UK

Abstract Alpine peatlands are one of the carbon reservoirs, provide vital ecosystem services, and support endangered biodiversity. However, they are globally understudied, including those in the Italian Alps, which host thousands of small sites averaging under 1 ha. Their complex geomorphology makes detection challenging with single-sensor, low-resolution remote sensing imagery. In the last decade, high resolution multi-source imagery (e.g., Sentinel series) and the cloud-based computation platforms (e.g., Google Earth Engine—GEE) have become available. Using these advancements, we developed a method to map the distribution of alpine peatlands. Utilizing 1 and 30 m digital elevation models (DEMs), optical, and microwave data sets, our method exploits a pixel-based Random Forest (RF) machine-learning algorithm on the GEE platform to map alpine peatlands in the Avisio River basin of the Italian Alps. The results show that the data set of single-year time series multi-source imagery, binary samples (peatland or non-peatland), and 30 m DEM is the most effective for mapping alpine peatlands. The method achieved an overall accuracy of 90.5%, with 81.8% true positives and 0.8% false positives. The method identified 11.635 km^2 of alpine peatlands, surpassing the 7.764 km^2 documented in official inventories, this discrepancy may be due to overestimation but also gaps in the existing reference inventory. In the classification process, DEM derived variables proved more effective than optical and microwave derived variables. Variable importance analysis in the RF model indicated that elevation is the most influential factor, while the microwave derived VV-VH difference (ascending track) contributes the least.

Plain Language Summary Alpine peatlands are globally underestimated, highlighting the need for effective and regularly updated mapping methods to better understand their distribution and extent. With advancements in remote sensing technology, large-scale mapping of alpine peatlands using satellite imagery has become increasingly feasible. While previous studies have achieved notable results using 30 m resolution satellite imagery, the performance and potential of 10 m resolution imagery have not been thoroughly validated. This study focused on mapping alpine peatlands within a specific river basin in the Italian Alps. We developed a mapping approach using 10 m resolution multi-source time-series remote sensing data from Sentinel-1 (microwave) and Sentinel-2 (optical) sensors, processed on the cloud-based Google Earth Engine platform, and applied a Random Forest image classification algorithm. The method demonstrated a high overall accuracy of 90.5%. Our findings indicate that variables derived from digital elevation models were more influential in the classification process than those derived from optical and microwave imagery. The alpine peatlands classification method can be extended to other regions, providing a valuable reference for mapping peatlands both within the Alps and in other similar environments.

Key Points:

- Using Random Forest to map alpine peatlands is effective when optical and microwave data are combined with hydrogeomorphological indices
- Alpine topography and geomorphology contribute more significantly to peatland identification than optical and microwave data
- The method achieves high overall accuracy, even the small size of peatlands and the mountainous topography facilitate the overestimation

Supporting Information:

Supporting Information may be found in the online version of this article.

Correspondence to:

Q. Li,
qiqi.li2@unibo.it

Citation:

Li, Q., Singh, M., & Silvestri, S. (2025). Remote sensing of alpine peatlands: Challenges of mapping thousands of sparse small sites scattered across extensive mountainous territories. *Earth and Space Science*, *12*, e2025EA004201. https://doi.org/10.1029/2025EA004201

Received 28 JAN 2025
Accepted 28 JUN 2025

Author Contributions:

Formal analysis: Qiqi Li
Methodology: Qiqi Li, Manudeo Singh, Sonia Silvestri
Resources: Sonia Silvestri
Software: Qiqi Li
Validation: Qiqi Li
Writing – original draft: Qiqi Li
Writing – review & editing: Qiqi Li, Manudeo Singh, Sonia Silvestri

1. Introduction

Peatlands are globally recognized for their capacity to provide ecosystem services for unique biodiversity and water regulation (Parish et al., 2008). But most importantly, peatlands are one of the largest terrestrial carbon reservoirs (Camill, 2005), storing 500–700 Gt of carbon, which likely exceeds the carbon content of terrestrial vegetation globally (~560 Gt) and comparable to the estimated size of the atmospheric carbon pool (~850 Gt) (Turetsky et al., 2020). When disturbed, peatlands emit large amounts of greenhouse gases (GHGs), particularly N_2O (Frolking et al., 2011), CH_4 (Strack et al., 2019), and CO_2 (Pullens et al., 2016). Moreover, the disturbance to peatland due to climate change causes an increase in wildfires in tropical (Ribeiro et al., 2021), sub-arctic, and arctic areas (Witze, 2020), and results in permafrost thaw (O'Neill et al., 2020). According to the prediction of

Turetsky et al. (2020), the abrupt thaw of permafrost will lead to a CO_2 emission of 3.1 Pg C per °C. On the other side, anthropogenic activities such as forestry exert pressure on peatlands, resulting in over 0.2–0.3 Pg C emissions annually (Frolking et al., 2011; Rowland et al., 2023).

Globally peatlands cover an area of about 4.88 million km^2, which is approximately 3.8% of the land surface (UNEP, 2022). In general, 75%–80% of peatlands occur in boreal and sub-arctic regions, about 10%–15% of them are in tropical areas, and around 10% are in temperate zones (Frolking et al., 2011). They can occur on plains, mountains, and other landscapes, with surface elevation ranging from 0 (Hendriks et al., 2007) to above 4,500 m (Hribljan et al., 2024).

Among the various ecosystems where peatlands develop, alpine ecological communities including alpine sphagnum bogs and associated fens are poorly documented globally (H. Chen et al., 2014; Grzybowski & Glińska-Lewczuk, 2020), which across alpine, subalpine and montane landscape. Those unaccounted alpine peatlands are primarily distributed in the Alps (Reichart, 2020), Himalayas (Khan et al., 2020), Andes Mountains (Valois et al., 2020), Australian Alps and Tasmania (Rowland et al., 2023), and the Tibetan Plateau (H. Chen et al., 2014). They are small, highly scattered (Carbognani et al., 2023; DEWHA, 2009), and being carbon reservoirs, at risk of feedback to climate change (Patthey et al., 2008). The harmonized World Soil Database (Fischer et al., 2008) and the global digital soil map SoilGrids250m (Hengl et al., 2017) are being regularly updated as well as other maps on the distribution of global peatlands produced by several researchers (Melton et al., 2022; Wu et al., 2017; Xu et al., 2018). However, peatlands in mountainous regions are often undifferentiated or misclassified (Chimner et al., 2019; Gumbricht et al., 2017). In Argentina, the peatland of Andes Mountain is mapped within the wider framework of mapping ecosystem types without distinguishing which wetland types have peat (UNEP, 2022). The Global Peatlands Assessment (GPA) data set produced by United Nations Environment Programme reports that there is still high inaccuracy on the correct and complete mapping of alpine peatlands in Andes Mountains, Australian Alps, and Central and southern European mountain compound region, including Alpine peatlands of Italy (UNEP, 2022).

Only a limited amount of research has delineated (Tanneberger & Belous, 2017) or pointed out (Martinelli et al., 2012) the distribution of Alpine peatlands in Italy. A recent attempt to map the peatlands in the Alps by Reichart (2020) could not include Italian peatlands citing challenges in accessing public data. Moreover, due to rapidly changing land use (Minasny et al., 2024), especially agricultural development (Cremonini et al., 2008), existing data may no longer be accurate. Furthermore, all existing maps for Italy lack comprehensiveness for peatlands with an uncertain estimated peatlands area ranging from 300 to 1,200 km^2 (Tanneberger & Belous, 2017). Overall, no specific and comprehensive map for Italian alpine peatlands is publicly available, resulting in a major handicap in peatland research.

Conventional approaches to mapping alpine peatlands typically involve field surveys and aerial photography and are characterized by long update cycles and considerable costs (Vitt et al., 2000). The location of alpine peatlands in inaccessible terrain, often surrounded by dense forests, makes field surveys challenging (Chimner et al., 2019). UAVs (unmanned aerial vehicles) offer flexibility and lower costs and provide additional valuable information as for example, the possibility of detecting vegetation species (Assiri et al., 2023), but with limited coverage. Using large scale satellite remote sensing imagery for alpine peatland extent mapping is an effective method (Izquierdo et al., 2015). At present, alpine peatlands extent mapping research is usually based on coarse resolution single-source optical (i.e., Landsat imagery) (Khan et al., 2020) or multi-source remote sensing images (e.g., Landsat imagery, ALOS PALSAR, SRTM DEM, and RADASAT-1) (Chimner et al., 2019; Hribljan et al., 2017) employing supervised classification algorithms to identify peatlands (Minasny et al., 2024). These studies have shown that: (a) remote sensing satellites with 30 m or lower spatial resolution have clear limitations in detecting small, individual areas of alpine peatlands (Minasny et al., 2019), and tend to overestimate the size of small land covers (Gallego, 2004); (b) single-source optical data has drawbacks, particularly in mountain regions with persistent cloud cover, making it difficult to obtain cloud-free images (Anaya et al., 2015; Hribljan et al., 2017); (c) non-peatland areas may floristically resemble peatlands, making them difficult to differentiate using only optical sensors (e.g., Landsat) (Hribljan et al., 2017; Steenvoorden & Limpens, 2023); (d) cloud-based geospatial analysis platforms such as Google Earth Engine (GEE) (Gorelick et al., 2017) have not been utilized in alpine peatland mapping research.

In Italy, the irregular shape and uneven distribution of thousands of small peatlands across the Alps (Carbognani et al., 2023; Pullens et al., 2016) with an average area of under 1 ha (Assiri et al., 2023; Q. Li et al., 2024a),

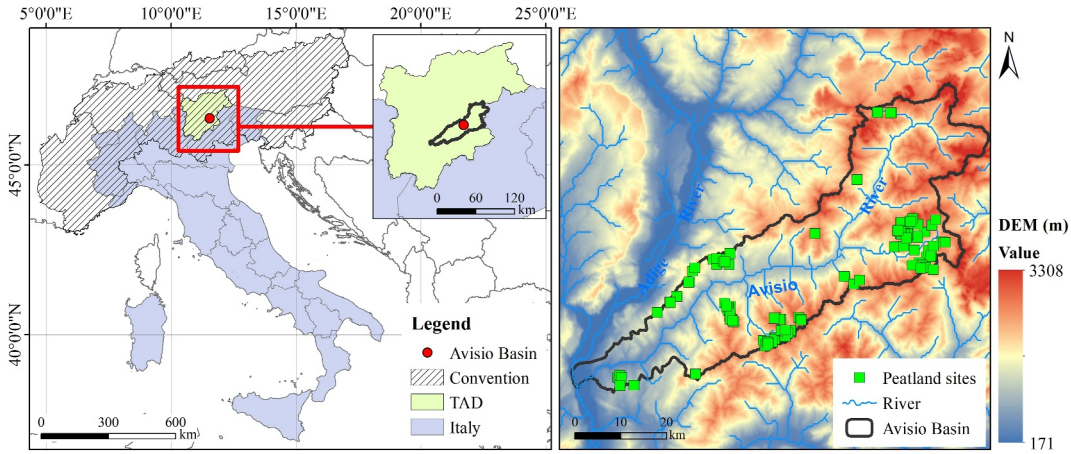

Figure 1. The location of Avisio basin. TAD means "Trentino-Alto Adige" region. The convention is Alps Alpine convention area.

necessitates the use of higher spatial resolution data sets to minimize overestimation (X. Sun et al., 2023). Another important challenge in retrieving these ecosystems is that some of the alpine peatlands are typically located in sloping valleys and they are surrounded by inclined terrain (Gerdol et al., 1994; Poto et al., 2013) that demands multi-source imagery to provide sufficient features.

The development of spatial resolution of multi-source satellite data and the advancement of remote sensing space computing technology in recent years have brought new opportunities for mapping alpine peatlands. The Copernicus mission has made Sentinel-1 and Sentinel-2 data freely available (https://sentinels.copernicus.eu/web/sentinel/missions). It provides microwave and optical remote sensing imagery with a spatial resolution of up to 10 m (Zeng et al., 2022), offering an opportunity to refine our understanding of the extent and status of alpine peatlands (Minasny et al., 2024). The GEE platform, combined with multi-source remote sensing data, has been applied to map peatlands occurring on plains (DeLancey et al., 2019). However, we could not find any study aiming at mapping alpine peatlands using GEE and satellite data. Moreover, previous research has shown that topographic variables derived from DEM data play a significant role and microwave derived variables contribute less in mapping peatlands occurring on plain (Millard, 2016; Millard & Richardson, 2013).

Therefore, considering the challenges and opportunities on mapping Italian Alpine peatlands, this study aims to explore a simple, effective, and easily reproducible mapping model using the GEE platform with Random Forest (RF) algorithm, based on multi-temporal Sentinel-1 and Sentinel-2 images and Digital Elevation Model (DEM) data. Specifically, the paper is structured as follows: Section 2 describes the study area, the data set used and the method employed; Section 3 presents the results; Section 4 discusses and highlights the main findings of the study as well as the limitations and is followed by the conclusion Section 5.

2. Materials and Methods

2.1. Study Area

The study area is situated within the Trentino-Alto Adige (TAD) region (Figure 1) (Runfola et al., 2020) and falls under the Alpine Convention Area (Balsiger, 2016),which is the world treaty under international law designed to protect a mountain region. As shown in Figure 1, the Avisio River delineates a basin covering an area of 1,984.95 km^2 (Manfreda & Fiorentino, 2008). Climatically, the annual mean precipitation of this area ranges from 1,000 to 1,600 mm, with an annual mean temperature spanning from −3.2°C in January to 14°C in July (Crespi et al., 2021). Geographically, the region primarily consists of mountainous terrain, ranging from 171 to 3,308 m in elevation (Figure 1).

Within this context, the Avisio Basin stands out as one of the areas with the highest amount of alpine peatland sites ranging from 1,310 m to 2,400 m, as recorded by both the Natura 2000 network, regional authority and other sources (Table S1 in Supporting Information S1) (Maiorano et al., 2007). Alpine peatland in this area includes bogs, fens and mires ecosystem (European Commission et al., 2008) with a minimum peat thickness of 30 cm

(Tanneberger & Belous, 2017). Alpine peatlands in this area are typically located in small valleys developed in the post-glacier period (Gerdol et al., 1994; Poto et al., 2013). Based on available records, the total peatland area is at least 7.764 km^2. However, it is possible that several sites surrounding the recorded peatland sites were neglected (Figure S1 in Supporting Information S1), resulting in a general underestimation of the total area of peatlands in the Avisio basin. The green squares (Figure 1) indicate the locations where peatlands were recorded within the Avisio Basin. The sites are not evenly distributed across the basin; rather, they are mainly concentrated in the southwestern and eastern sectors of the study area.

2.2. Documented Peatland Sites

The peatland database was created by merging data from various sources, including inventories provided by the regional authority and the Natura 2000 network (see Table S1 in Supporting Information S1 for detailed information on sources and links). To refine the information on peatlands within the available inventories, we used keywords such as "peat," "fens," "bogs" (European Commission et al., 2008). The inventory includes 293 peatland sites, with a total documented area of 7.764 km^2. All 293 peatland sites were overlaid on Google imagery from 2023 using the Google Earth plugin in QGIS Desktop 3.22.13. The locations and boundaries of existing sites were manually digitized and updated through visual inspection. Forested areas were excluded from some of the sites, thus retaining only areas with low-vegetation typical of alpine peatlands. This process was necessary to minimize the uncertainty that forested lands would introduce into the recognition process. Therefore, we extracted a total of 165 peatland sites (Figure 1). These sites varied in area from 0.002 km^2 to 0.0463 km^2, with an average area of 0.007 km^2. Additionally, to create the "non-peatland" data set, a total of 292 regions of interest were digitized using Google Earth plugin in QGIS Desktop 3.22.13. These regions were selected over the following land-cover categories: vegetation (90 sites), water bodies (32 sites), construction land (65 sites), snow-covered areas (24 sites), and bare land (81 sites).

2.3. Remote Sensing Data and Products

2.3.1. Multi-Sensor Remote Sensing Data Preprocessing

We selected a total of 635 scenes of Sentinel-1 (S1) SAR (Synthetic Aperture Radar) and 526 scenes of Sentinel-2 (S2) MSI (Multispectral Instrument) images from the data catalogue of the GEE platform, spanning the snow-free months (Pullens et al., 2016) from May to September of 2020–2022. We collected and analyzed the images from three consecutive years to enable a comparative analysis of classification effectiveness against single-year classification approaches.

For S1, we chose both ascending and descending orbits and used VV and VH backscatters of the Interferometric Wide (IW) observation mode (Table 1) of both orbits separately. Following Torres et al. (2012), we computed the VV and VH difference, that is, VV − VH of each S1 scene of both orbits (Table 1). We used S2 Level-2A surface reflectance scenes with less than 10% cloud coverage, and both the 10 and 20 m spectral bands (i.e., B2 to B8, B8A, SWIR1, and SWIR2), resampling the 20 m bands to 10 m resolution using the nearest neighbor interpolation (Table 1). Additionally, we computed five indices for each S2 scene to enhance the information on vegetation, water and soil moisture: Normalized Difference Vegetation Index (NDVI), Enhanced Vegetation Index (EVI), Normalized Difference Water Index (NDWI), Normalized Difference Snow Index (NDSI), Shortwave infrared transformed reflection (STR) (Table 1). We generated a monthly mean of all S1 and S2 derived variables by computing the arithmetic mean of all available data for each month. This resulted in 5 monthly images per year for a total of 15 images for each variable in the 3-year period.

2.3.2. Topographic and Hydrological Variables

In addition to S1 and S2 data derived variables (Table 1), we used two different DEM data to compare the influence of spatial resolution: (a) Copernicus DEM (GLO-30) (European Space Agency, 2024) with a spatial resolution of 30 m and (b) airborne derived LiDAR data (access online at: https://siat.provincia.tn.it/stem/) with a spatial resolution of 1 m (Table 1). To maintain consistency with other variables used in this study (Table 1), GLO-30 and LiDAR data were both resampled to a spatial resolution of 10 m using cubic convolution resampling method. Subsequently, using the resampled DEMs, we applied depression filling preprocessing on the data using SAGA GIS 7.8.2 and calculated slope and several topographic and hydrological indices (Tables 1 and 2). Formulas and descriptions of the topographic indices, that is, Channel Network Baselevel (CHNL_BASE), Channel

Table 1
List of Variables Derived From Sentinel-1, Sentinel-2 Data and DEMs

Sensor and scenes count	Variables	Resolution	Definition and reference
Sentinel-1	IW mode/dual polarization bands	10 m	VV, VH ascending (Relative orbit number: 117 and 44)
125 scenes (ascending)			VV, VH descending (Relative orbit number: 168 and 95)
126 scenes (descending)			
Sentinel-2	Spectral bands	10 m	VV-VH difference ascending and descending Blue, Green, Red, NIR (Tiles: 32TPS and 32TQS)
29 scenes		20 m	Vegetation Red Edge (i.e., B5, B6, B7, B8A), SWIR1, SWIR2
	Normalized Difference Vegetation Index (NDVI)	10 m	$(NIR - Red) / (NIR + Red)$[a]
	Enhanced Vegetation Index (EVI)	10 m	$2.5 \times (NIR - Red) / (NIR + 6 \times Red - 7.5 \times Blue + 1)$[b]
	Normalized Difference Water Index (NDWI)	10 m	$(NIR - SWIR2) / (NIR + SWIR2)$[c]
	Normalized Difference Snow Index (NDSI)	10 m	$(Green - SWIR1) / (Green + SWIR1)$[d]
	Shortwave infrared transformed reflection (STR)	10 m	$(1 - SWIR2)^2 / (2 \times SWIR2)$[e]
GLO-30	DEM	30 m	Elevation, Slope, and other topographic and hydrological variables (Section 2.3.2)
LiDAR Data	DEM	1 m	Elevation, Slope, and other topographic and hydrological variables (Table 2)

Note. Sentinel-1 and Sentinel-2 include observations performed for 5 months (May–September) for each considered year, that is, 2020, 2021, and 2022. The date of each scenes is displayed in Table S2 in Supporting Information S1. Topographic and hydrological variables are derived from DEM products. [a]Rouse et al. (1974). [b]Huete et al. (2002). [c]Gao (1996). [d]Hall et al. (1995). [e]Sadeghi et al. (2017).

Network Distance (CHNL_DIST), Terrain Surface Texture (TEXTURE), LS-Factor (LS), Relative Slope Position (RSP), Wetness Index (WETNESS), Profile Curvature (VCURV), Plan Curvature (HCURV), and Convergence (Conrad et al., 2015) are shown in Table 2. These indices can help understand various geomorphological and hydrological processes highly related to alpine peatlands development, such as habitat suitability and water flow. Additionally, we computed a hydrological connectivity index (IC) (Cavalli et al., 2013), the detailed computation and formula are shown in Supporting Information S1 (Figure S2). The IC represents the potential sediment connectivity characteristics within a small alpine catchment (Martini et al., 2022). The connectivity concept and IC have been used previously in other low-energy systems such as wetlands elsewhere (Singh et al., 2022; Singh & Sinha, 2022). Calculations were performed using the IC R package developed by Martini et al. (2022).

2.4. Pixel-Based Classification and Validation Process

We applied a pixel-based RF algorithm on the GEE platform, using multi-source and time series imageries (Tables 1 and 2), as shown in the flowchart (Figure 2). We first prepared multi-source remote sensing imagery products, as described in the previous section. Two data sets were created using features extracted from both S1 and S2 images: one data set utilized images collected in a single year (year 2022), while the second data set used images collected over a 3-year period (years 2020–2022). For each of the two data sets, topographic and hydrological features were derived from the GLO-30 DEM for first iteration and from LiDAR data for the second iteration.

We computed statistics on the influence of slope on peatland presence using known peatland sites (Section 2.2) and generated a mask to exclude territories unsuitable for peat accumulation. The slope analysis revealed that peatlands included in the official inventory occur on flat to slightly sloping terrains, with a maximum slope value of 17° recorded for peatlands in the Avisio Basin (Figure S3 in Supporting Information S1). Based on these result, we defined a mask encompassing exclusively lands with slopes between 0 and 17° (Figure S4 in Supporting Information S1), thus excluding most of the territory from further analyses and retaining only 32.6% of the total

Table 2
The Definition of Topographic and Hydrological Indices in the Study

Indices	Definition and reference
Channel Network Baselevel (CHNL_BASE)	$B = \min(E(x))$ where B is the base level. $E(x)$ is the elevation profile function of the river along its course x[a]. The CHNL_BASE represents the minimum elevations of a channel network
Channel Network Distance (CHNL_DIST)	$D = \sum_{i=1}^{n} L_i$ where L_i is the length of each channel segment within the network, n is the total number of channel segments[a]. The CHNL_DIST represents the distance along the channel network from each cell to the nearest channel network cell
Terrain Surface Texture (TEXTURE)	$T = \sqrt{\frac{1}{N}\sum_{i=1}^{N}(h_i - \overline{h})^2}$ where N is the total number of height measurements or sample points, h_i is the height of the terrain at the i-th sample point. $\overline{h}$ is the mean height of the terrain surface[b]. The TEXTURE measures the variation and roughness of the ground surface
LS-Factor (LS)	$\mathrm{LS} = \left(\frac{m}{22.1}\right)^{0.4}\left(\frac{s}{0.0896}\right)^{1.3}$ where m is the slope length in meters, S is the slope steepness or gradient in percent (rise over run, expressed as a percentage)[c]. The LS represents the combined effect of slope length and slope steepness on soil erosion[c]
Relative Slope Position (RSP)	$\mathrm{RSP} = \frac{h - h_{\min}}{h_{\max} - h_{\min}} \times 100$ where h is the elevation or height of the point of interest. $h_{\min}$ is the minimum elevation in the neighborhood around the point. $h_{\max}$ is the maximum elevation in the same neighborhood[d]. The RSP is a crucial topographic aspect in peatland studies, influencing factors like erosion, and sediment transport
Wetness Index (WETNESS)	$\mathrm{WETNESS} = \ln\left(\frac{A}{\tan\beta}\right)$ where A is the contributing area, which represents the upslope contributing area to a point on the terrain surface. It is often calculated using algorithms that simulate surface water flow accumulation. β is the slope gradient[d]. The WETNESS is a significant parameter used in hydrological analysis to assess the tendency of an area to accumulate water
Profile Curvature (VCURV)	$C_p = -\frac{d^2z}{dx^2}\left(1 + \left(\frac{dz}{dx}\right)^2\right)^{-\frac{3}{2}}$ where z is the elevation of the terrain surface. x is the horizontal distance along the profile. $\frac{dz}{dx}$ represents the slope gradient (first derivative of elevation with respect to distance). $\frac{d^2z}{dx^2}$ represents the second derivative of elevation with respect to distance, which describes the curvature of the profile[e,f]. The VCURV quantifies the topographic influence on hydrological processes by considering both slope and the upstream contributing area per unit width orthogonal to the flow direction
Plan Curvature (HCURV)	$C_{\mathrm{pl}} = -\frac{d^2z}{dy^2}\left(1 + \left(\frac{dz}{dx}\right)^2\right)^{-\frac{3}{2}}$ where z is the elevation of the terrain surface. x and y are the horizontal and vertical coordinates, respectively. $\frac{dz}{dx}$ and $\frac{d^2z}{dy^2}$ represent the first and second derivatives of elevation with respect to x and y, respectively[e,f]. The HCURV reflects the rate of change in aspect along a contour line and is crucial for understanding flow convergence or divergence within a landscape
Convergence	$\mathrm{Convergence} = -\tan(\alpha)\cdot\frac{W}{A}$ where α is the slope angle. W is the contour length perpendicular to the flow direction. A is the upslope contributing area. Convergence typically occurs in valleys or depressions where water from surrounding areas converges toward a central point, which is critical information in understanding hydrological processes, especially in relation to water flow[a,g]

[a]Olaya and Conrad (2009). [b]Iwahashi and Pike (2007). [c]Kinnell (2005). [d]Böhner and Selige (2006). [e]Wood (1996). [f]Wood (2009). [g]Conrad et al. (2015).

basin research area for subsequent computations. This mask significantly reduces the data volume and precessing area, improving computation time.

Next, we input object variable images and training samples into RF algorithm. We computed the results, performed a variable importance (VI) analysis to assess the contribution of each variable, and validated the results. We repeated these steps using different remote sensing imagery time series lengths and spatial resolutions of DEM. Finally, we post-processed the classified results to reduce the noise in the predicted peatland map by

10.1029/2025EA004201

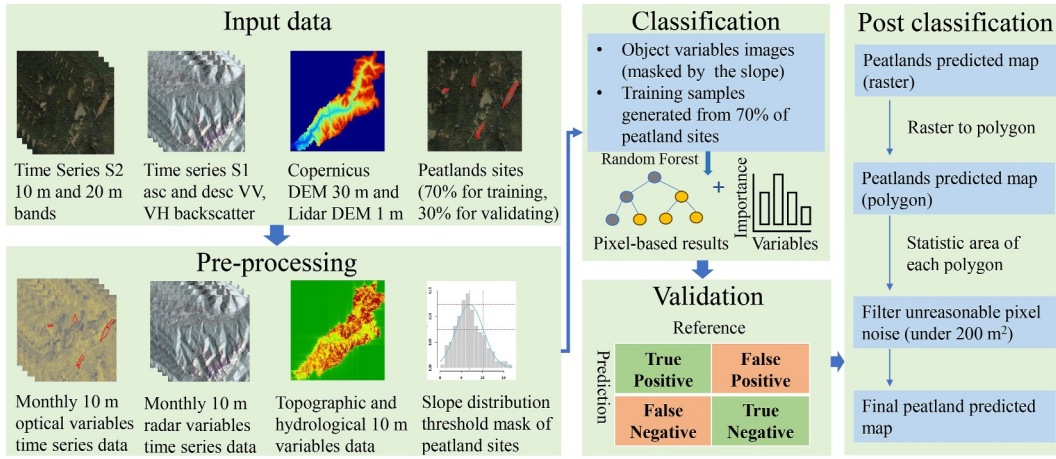

Figure 2. Flowchart of the methodology.

removing all sites comprising less than three pixels in the predicted peatland map (Text S3), thereby retaining only sites larger than 200 m^2 (Figures S5 and S6 in Supporting Information S1).

The Random Forest (RF) algorithm (Breiman, 2001) is renowned for its outstanding performance in classification and computational efficiency (Belgiu & Drăguţ, 2016; Rodriguez-Galiano et al., 2012). The RF algorithm was implemented using the "smileRandomForest" classifier on the GEE platform. A binary classification was performed, distinguishing between "peatland" and "non-peatland" categories, based on the data sets described in Section 2.2. To enable a final validation phase—used to calculate True Positives (TP), False Positives (FP), True Negatives (TN), and False Negatives (FN)—we randomly set aside 30% of the peatland sites and 30% of the non-peatland sites prior to applying the RF algorithm. The RF classification was subsequently applied to the remaining 70% of the sites. To guaranty a representative and balanced sampling while ensuring sufficient training data for "peatland" and "non-peatland" classes. We applied the downsampling method (Lee & Seo, 2022) with the "sampleRegions" function provided by GEE for majority land covers (i.e., non-peatland class). For "peatland" areas, we sampled at 10 m scale, while for "non-peatland" areas, we sampled at 30 m scale. This resulted in 106 peatland sites (corresponding to 4,585 sample pixels) and 206 non-peatland sites (corresponding to 5,966 sample pixels). The bag fraction of input data per tree was set at 0.7, meaning the RF algorithm iteratively used 70% of the training sample data set while the remaining 30% was used to provide the out-of-bag (OOB) error evaluation of the model. After iteratively testing the algorithm with an increasing number of trees, we set the number of 600, as the accuracy tended to stabilize beyond this point (Figure S7 in Supporting Information S1). To quantify the accuracy of the RF calibration, we computed the OOB error, which is the percentage of samples that are incorrectly predicted in OOB to the total samples.

For validation, from the 30% of sites set aside at the beginning, we randomly selected 1,000 pixels each for the peatland and non-peatland categories using the "Random Points Inside Polygons" tool in QGIS Desktop 3.22.13. Subsequently, to quantify the accuracy of the results, we computed the confusion matrix extracting the Overall Accuracy (OA) and Kappa coefficient. We also assessed the percentage of True positives (TPs, i.e. true ground peatland correctly labeled as peatland), and False positives (FPs, i.e. non-peatland incorrectly labeled as peatland). The higher TPs, the more alpine peatlands can be detected. However, the higher FPs, the more non-peatland land covers can be misclassified as alpine peatlands. Simultaneously, we calculated the positive predictive values (PPV) to evaluate proportions of positive results in all prediction positive instances. The higher PPV indicates fewer misclassifications will appear in the results (X. Sun et al., 2023). To minimize the misclassified peatlands, the study focuses on lower FPs and higher PPV:

$$\mathrm{PPV} = \frac{\mathrm{TP}}{\mathrm{TP} + \mathrm{FP}} \tag{1}$$

where PPV is the proportions of positive results in statistics and diagnostic tests that are true positive results. TP and FP are the percentage of True positives and False positives of the confusion matrix, respectively.

2.4.1. Random Forest Variable Importance Analysis

The VI analysis is a method that allows the interpretation of the classification results and ranking the contribution of variables. We evaluated the Decrease Gini Impurity ($\Delta\text{Gini}(\tau)$) to measure the contribution of each variable among all those used for the classification. The Decrease Gini Importance (I_g) is the $\Delta\text{Gini}(\tau)$ for each variable θ across all decision trees T and all nodes τ (Menze et al., 2009). A higher I_g indicates that a variable θ has a greater contribution to reducing $\text{Gini}(\tau)$, making it more important as a variable, as described in the following equations:

$$\text{Gini}(\tau) = 1 - \sum_{i=1}^{k} {p_i}^2 \tag{2}$$

$$\Delta\text{Gini}(\tau) = \text{Gini}(\tau) - p_l\text{Gini}(\tau_l) - p_r\text{Gini}(\tau_r) \tag{3}$$

$$I_g(\theta) = \sum_{T}\sum_{\tau} \Delta\text{Gini}_\theta(\tau, T) \tag{4}$$

where $p_i = \frac{n_k}{n}$ is the fraction of the n_k samples from class $k = \{1, 2, 3\ldots, i\}$ out of the total of n samples at node τ, l, and r are the left and right child nodes after splitting node τ, respectively.

Finally, to establish the actual contribution provided by the DEM, optical and microwave derived variables, we performed the classification with a different selection of data sources with the following iterations: (a) DEM; (b) DEM and optical; (c) DEM, optical and microwave, and validated results of each iteration using the 2000 points which were mentioned in Section 2.4. The three iterations conducted for this final analysis utilized the 30 m DEM (i.e., GLO-30) and single-year imagery, as this combination proved to be the most effective for classification, as detailed in the following sections.

3. Results

3.1. Single-Year Data-Based Peatlands Mapping

The peatlands mapping and validation results of the single-year data of 2022 are shown in Figure 3 and Table 3. Two zoomed-in example sites (Figure 3) show the predicted peatlands overlaid on the ground truth peatland sites documented in the official inventories (Section 2.2). Most predicted peatlands present in Figure 3 are concentrated in the eastern part of the basin, with a few in the northwest and south. The spatial distribution largely aligns with the documented peatlands patterns, except in the northwest region (Figures 1 and 3).

The zoomed-in plot shows that Binary_GLO-30 in Site A identified two additional documented peatland sites compared to Binary_LiDAR classification. In site A, tree-covered areas are misclassified as peatlands by both classification approaches, based on our visual judgment using Google Earth images (Figure 3). In Site B, both approaches detect all documented peatlands. However, Binary_LiDAR misclassify other land covers as peatlands more than Binary_GLO-30 (Figure 3), increasing FPs (Table 3).

As shown in Table 3, the Kappa values for all single-year classification outcomes exceed 0.77. This is considered a strong result, as a Kappa coefficient between 0.60 and 0.80 indicates substantial agreement, supporting the interpretation of high reliability (Cohen, 1960; Wan et al., 2015). The confusion matrix of single-year results (Table 3) indicates that the difference of 10 m DEM derived from GLO-30 and LiDAR DEM does not significantly impact the accuracy of the results. Specifically, compared to the GLO-30 DEM, there is an increase in FPs by 0.3% and a decrease in OA, PPV, and TPs by 2.1%, 0.4%, and 3.9% respectively when using LiDAR DEM data. Thus, the influence of finer spatial resolution of the DEM data on the classification results is considered negligible. Moreover, the estimated areas of peatlands across different classifications are similar. The classification with GLO-30 data predicts an area of 11.635 km^2, while the LiDAR classification estimates 11.268 km^2. Both classifications show a positive deviation compared to the documented area of 7.764 km^2.

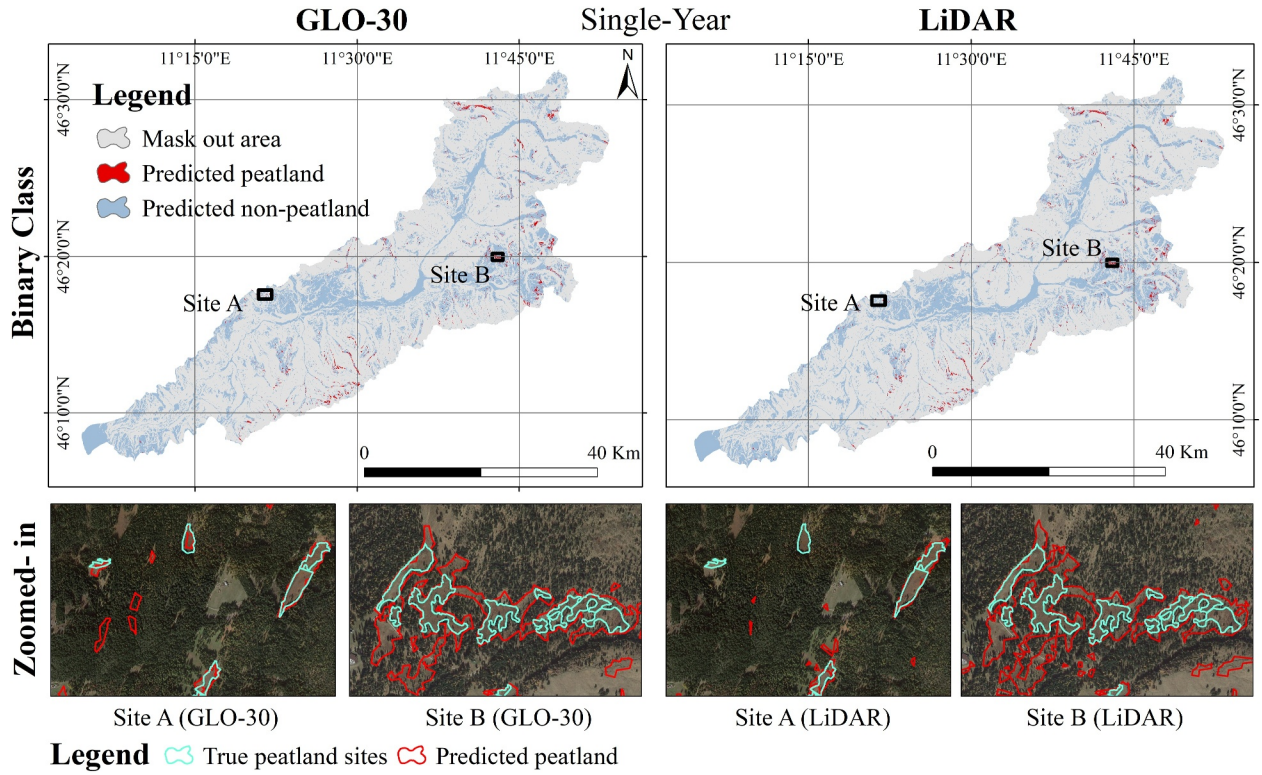

Figure 3. Peatland mapping using single-year data-based classification. The mask out area is the area with slope larger than 17°. Predicted peatland and non-peatland are the result of the RF. True peatland sites are retrieved from the official inventories and digitized for this work (Section 2.2).

3.2. Multi-Year Data-Based Peatlands Mapping

Figure 4 shows the distribution of peatland and non-peatland areas retrieved with the multi-year approach as well as the zoomed-in maps of Site A and Site B. Visually, the overall spatial distribution of predicted peatlands using multi-year time series is similar to the results of single-year time series. However, sites A and B show different results compared to the single-year data-based approach. At Site A, the multi-year Binary_GLO-30 approach misclassifies fewer non-peatland areas as peatlands but fails to identify the westernmost documented peatland sites. The multi-year Binary_LiDAR reduces misclassification of non-peatland land covers and identifies an additional documented peatland site (Figures 3 and 4). At Site B, the multi-year Binary_GLO-30 overestimates peatlands extent compared to the single-year approach, whereas the multi-year Binary_LiDAR performs similar to the single-year approach.

As depicted in Table 3, the Kappa of all outcomes in multi-year classification is larger than 0.75. However, the accuracy assessment results show that using multi-year remote sensing imagery does not lead to a notable improvement in peatland detection compared to the single-year results (Figure 4; Tables 3 and 4). Moreover, we notice that there is an increase in FPs and a decrease in PPV when using multi-year time series imagery. For

Table 3
Accuracy Calibration of RF Performance and Classification Validation Results of Single-Year Iteration

	RF performance	Classification validation					
Single-year	OOB (%)	OA (%)	Kappa	TPs (%)	FPs (%)	PPV (%)	Areas (km^2)
Binary_GLO-30	0.33	90.5	0.81	81.8	0.80	99.0	11.635
Binary_LiDAR	0.34	88.4	0.77	77.9	1.10	98.6	11.268

Note. OA is overall accuracy. TPs and FPs are true positive and false positive, respectively. PPV is positive predictive value, which is the ratio of TPs in all predicted positive instances. OOB is out of bag error for RF. Areas are the extent of predicted peatlands.

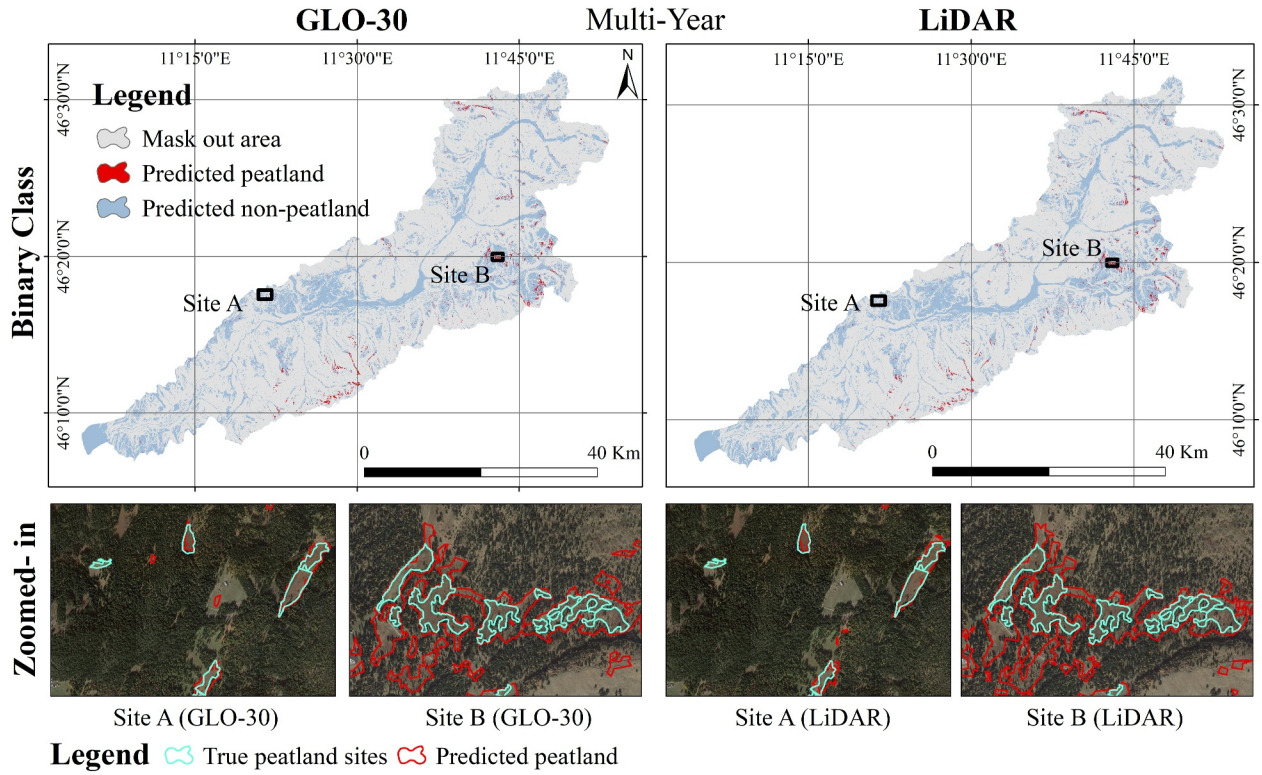

Figure 4. Peatland mapping using multi-year data-based classification. The mask out area is the area with a slope larger than 17°. Predicted peatland and non-peatland are the result of the RF. True peatland sites are retrieved from the official inventories and digitized for this work (Section 2.2).

example, in the classification that uses GLO-30 DEM, although the TPs increase by 3%, the FPs increase by 0.7%, and the PPV decreases by 0.8%. Meanwhile, the positive deviation between the predicted peatland extent from the multi-year classifications and the documented peatlands area is greater than that observed in the single-year classification results (Tables 3 and 4). Similar to the single-year classification, the difference between the 10 m DEM derived from GLO-30 and LiDAR does not significantly affect accuracy. Specifically, compared to GLO-30 DEM, there is a slight increase in TPs and FPs by 0.3%, and 0.6% respectively with a decrease in OA and PPV by 1.3%, and 0.5% respectively when using LiDAR DEM data.

3.3. Importance of Random Forest Variables

We select the single-year "Binary_GLO-30" result for the VI analysis, as it performs well across all approaches (Tables 3 and 4). Based on the Decrease Gini Impurity Importance during the RF classification (Figure 5). We notice that DEM derived topographic variables exhibit the highest contribution, followed by the optical and microwave remote sensing derived variables. Among all variables, the top three contributors are ELEVATION, CHNL_BASE, and CHNL_DIST.

Table 4
Accuracy Calibration of RF Performance and Classification Validation Results of Multi-Year Iteration

	RF performance	Classification validation					
Multi-year	OBB (%)	Kappa	TPs (%)	FPs (%)	PPV (%)	OA (%)	Areas (km^2)
Binary_GLO-30	0.31	0.83	84.8	1.50	98.2	91.7	11.915
Binary_LiDAR	0.35	0.81	87.8	2.10	97.7	90.4	11.811

Note. OA is overall accuracy. TPs and FPs are true positives and false positives, respectively. PPV is positive predictive value, which is the ratio of TPs in all predicted positive instances. OOB is out of bag error for RF. Areas are the extent of predicted peatlands.

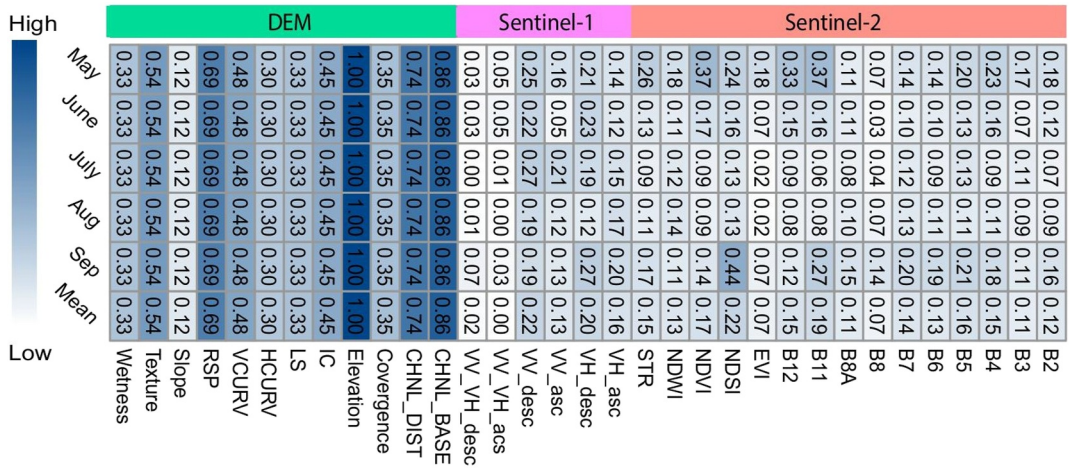

Figure 5. The normalized Gini impurity importance score of the variables retrieved with the random forest classification process. The *x* axis is the list of variables, the abbreviations are Channel Network Baselevel (CHNL_BASE), Channel Network Distance (CHNL_DIST), Terrain Surface Texture (TEXTURE), LS-Factor (LS), Relative Slope Position (RSP), Wetness Index (WETNESS), Profile Curvature (VCURV), Plan Curvature (HCURV), and hydrological connectivity index (IC). The *y* axis shows the month, while "Mean" is the mean importance value from May to September. The DEM derived topographic variables do not change overtime and share the same values each month.

The contribution of variables derived from optical images is significantly lower than the topographic variables. For example, the average importance of variables such as NDVI and STR, which can reflect the vegetation photosynthetic capacity and moisture characteristics of peatlands, is only 17% and 15%, respectively. In general, the importance of optical variables does not exceed 50% in terms of VI with seasonal variation.

The VI of microwave derived variables is found to be the least in this study, ranging from 0% to 22%. The highest VI of microwave variables is for the descending VV backscatter. The lowest VI is the ascending VV-VH difference backscatter. The contribution of ascending and descending backscatter coefficients of VV is similar to that of optical variables. The contribution of both ascending and descending VV-VH difference backscatter coefficients to the classification is almost negligible.

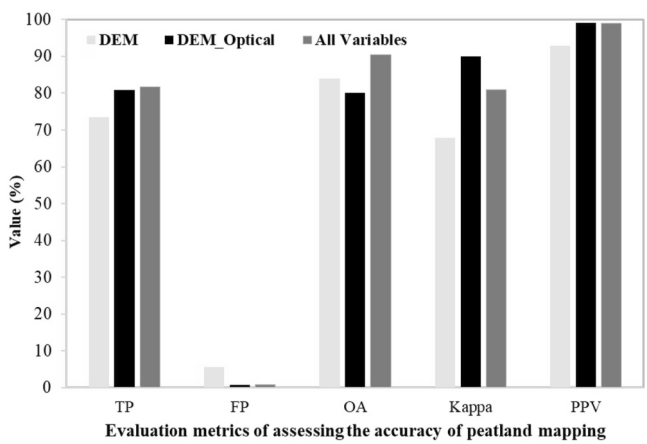

Figure 6. Accuracy parameters of selected classifications. "DEM" means variables only derived from 30 m DEM data. "DEM_Optical" means variables from 30 m DEM and optical images. "All variables" mean variables from 30 m DEM, optical, and microwave data sets. TPs, FPs, and OA mean true positives, false positives, and overall accuracy, respectively. PPV is positive predictive values, which is the ratio of TPs in all predicted positive instances.

As shown in Figure 6, there are high FPs when the variables are only from DEM. Moreover, the consistency of mapping results is relatively low, with a Kappa coefficient of 0.69. The advantage of optical images is confirmed by the classification of DEM_Optical iteration, with a noticeable decrease in FPs and an increase in TPs and PPV to the iteration with DEM only variables (Figure 6). Moreover, the Kappa coefficient increased from 0.69 to 0.9. This indicates that although the contribution of optical remote sensing to mapping peatlands is small, it is indispensable.

It is noteworthy that, in our case, microwave derived variables did not provide significant classification improvements in accuracy. When included, there is a slight increase in TPs but no change in FPs (Figure 6). However, the microwave variables led to the highest PPV values, even though the Kappa coefficient decreased to 0.81 (which is however within the acceptable range).

4. Discussion

Alpine peatlands are understudied, partly due to their location at high altitudes and in difficult-to-access areas. They are often hidden in valleys and surrounded by mountain peaks and forests. Although remote sensing can help overcome some accessibility challenges, mapping these peatlands remains difficult because they are typically small (averaging under 1 ha) and sparsely scattered across vast mountainous regions. Additionally, the presence of slopes

and forested lands can complicate the remote sensing mapping methods, potentially affecting accuracy. For these reasons, this study employed a multi-sensor approach and conducted a comprehensive evaluation of the various factors influencing peatland mapping, including different time series lengths of remote sensing images (of 1 and 3 years) and spatial resolution of DEMs.

4.1. Topographic Variables Dominance in Peatland Mapping

The main finding of this study is that DEM and topographic variables derived from DEM play the most crucial role in classification effectiveness (Figures 5 and 6). The importance of topographic variables surpasses that of variables derived from optical and microwave imagery. This is clear when we examine the importance ranking of variables shown in Figure 5, where the topographic variables rank and the most important factors. A peatland is formed by a layer of peat soil deeper than 30 cm (Frolking et al., 2011). It is known that the distribution of organic matter content of soil properties varies with topographic attributes (Dessalegn et al., 2014). Several studies have shown that topography plays a dominant role in soil properties, as the complexity of topography affects factors related to soil development, including vegetation communities, runoff, drainage, and microclimate (Miller et al., 1988; Wang et al., 2001). Therefore, the distribution of peat soil is highly correlated with topography (J. Sun et al., 2023). This feature is an important criterion for identifying peatlands using remote sensing images.

The importance of topographic variables and DEM in peatland classification has been shown by other studies. Millard and Richardson (2013) and Millard (2016) confirm that topographic variables derived from DEM are more important to mapping northern peatlands located in Canada, including open bogs, treed bogs and fens, than optical and microwave derived variables. A. Li et al. (2022) and Räsänen et al. (2020), emphasize the crucial importance of elevation in peatland classification, as well as the significant role of Terrain Surface Texture factors.

Our results suggest that topographic variables play a more crucial role than variables reflecting hydrological conditions, as for example, the hydrological connectivity index (IC). This is probably related to the complex morphology of Alps, where peatland areas develop within glacial and karst basins or tectonic depressions (Zilioli et al., 2011). In these locations, the IC value within peatlands are heterogeneous (Figure S2 in Supporting Information S1). This inhomogeneity may be due to the differing hydrological conditions between fens, which are supplied with water from ground or surface sources, and bogs, which rely solely on rainfall and snow for water supply (Amani et al., 2019). Another possible reason is that alpine peatlands typically have small surface areas, which makes it difficult to accurately calculate hydrological variables using DEMs (Bechtel & Goldscheider, 2017).

4.2. Effect of DEM Spatial Resolution and Imagery Time Series Length on Accuracy

Based on the analysis conducted in this study, the difference between 10 m DEMs derived from the down-sampling of 1 m LiDAR DEM and upsampling of 30 m GLO-30 has a negligible impact on the accuracy of peatlands mapping classification. Our results suggest that the 10 DEM derived from LiDAR does not significantly improve the classification accuracy compared to the 10 m DEM derived from GLO-30 DEM (Table 3; Table 4). The LiDAR derived DEM data may even decrease OA, TPs and PPV scores, and this may be related to the noise associated with very high spatial resolution, which amplifies local errors (Dai et al., 2019). Not only in mapping alpine peatlands, but higher spatial resolution DEM does not always produce higher precision in other related research areas. Kariminejad et al. (2020) reports that 5 m resolution DEM performs better than 1 m resolution DEM on collapsed pipe sites mapping. Z. Chen et al. (2020) finds that 70 m resolution DEM performs better than 30 m DEM for landslide susceptibility assessment. The selection of an appropriate DEM resolution is important for specific research issues. Therefore, consistent with previous studies that efficiently used 30 m DEM data to estimate and identify peatlands distribution (Chimner et al., 2019; Li et al., 2022), we confirm that using the 10 m DEM derived from LiDAR is unnecessary for our study.

Extent, size, and location of peatlands are stable for decades (van der Velde et al., 2021). Consequently, the information provided to the classification by single-year or multi-year remote sensing imagery turned out to be spectrally similar (Figure S8 in Supporting Information S1). This similarity likely contributed to the single-year approach resulting fewer FPs and a higher PPV compared to the multi-year approach (Figures 3 and 4; Tables 3 and 4). Nevertheless, it is worth noting that in the monitoring of peatland degradation (Brown et al., 2023) and research on peatland carbon balance (Nugent et al., 2018), multi-year time series remote sensing data provide valuable insights that single-year data may not capture. Additionally, time series remote sensing images can be

applied to classify different types of peatlands. Amani et al. (2017) successfully differentiated fens and bogs based on the spectral differences in indices series specific to various peatland types. In summary, although multi-year time series remote sensing imagery can provide more information, single-year imagery was sufficient for peatland identification in our case study.

Moreover, the Random Forst classifier is sensitive to sample design (Jin et al., 2014). Therefore, it is important to assess the impact of sampling strategy and class imbalance on RF classification performance. This consideration becomes even more critical given that generating both peatland and non-peatland training samples across large natural areas is a time-consuming and subjective process (Ghimire et al., 2012). Based on our sampling design research and experimentation (see Text S1 in Supporting Information S1), we recommend binary classification as the most effective approach, supported by comparative results with the multi-class model (Tables S3 and S4 in Supporting Information S1). In alpine regions, collecting a large number of training samples for all land cover classes is extremely challenging, particularly for underrepresented classes. Although the results obtained using a multi-class approach were deemed acceptable (Tables S3 and S4 in Supporting Information S1), we believe that, due to the imbalanced training data set, these results are inferior to those achieved with the binary classification approach. This is not an isolated case; Dalponte et al. (2012) found that RF classifier fails to cope with imbalanced training data. Du et al. (2015) found that the increasing size of training samples can effectively improve the RF classification accuracy. In summary, the 10 m DEM derived from GLO-30 DEM, single-year time series imagery, and binary sample are found to most effective in our study.

4.3. Assessment of Physical Interpretability of Optical and Microwave-Derived Variables

The development of peatlands is typically characterized by specific vegetation genera (e.g., sphagnum moss), with water being a necessary condition for their formation (Steenvoorden & Limpens, 2023). The specific properties of peatlands should distinguish them from other land covers, particularly vegetated land covers. However, in alpine regions, non-peatland soils covered by vegetation tend to consistently remain at cryic temperatures (mean annual temperature >0 and <8°C) and maintain high moisture levels throughout the year, as rainfall exceeds evaporation (Soil Survey Staff 2014; Zilioli et al., 2011). This similarity in moisture levels causes vegetated non-peatland soils and actual peatlands to have similar physical reflectance characteristics. Sphagnum moss and other peatland species may have similar phenological characteristics as other non-peatland species, making it difficult to capture the differences in their signals using 10 m optical remote sensing imagery (Q. Li et al., 2021; Räsänen & Virtanen, 2019). Moreover, even though the C-band backscatter of S1 is sensitive to soil moisture (Zeyliger et al., 2022), it is reported that the correlation between backscatter signals and soil moisture is strong only on bare land surfaces, and the interference of vegetation adds complexity to this relationship (Garroway et al., 2011). Our results suggest that the backscatter from S1 is unable to properly detect wetness beneath the vegetation canopy in the alpine peatlands. Furthermore, SAR imagery is particularly prone to geometric distortions in areas with high mountains and deep valleys, due to foreshortening, layover, enhanced resolution, and shadow (Samuele et al., 2021; Uemoto et al., 2018). The artifacts on mountain slopes and incidence angle interaction may produce radio frequency interference (RFI) (Tao et al., 2021), resulting in incorrect backscatter information. Multi-temporal mean filtering is one potential approach to mitigate RFI. However, our experiments show that extending the temporal mean filtering to 5 months did not improve the accuracy of classification in this study. Incorporating SAR data from different platforms with multiple aspect angles (Onojeghuo et al., 2021) may reduce terrain effects, but this is beyond the scope of our Sentinel-focused study.

4.4. Study Limitations and Future Potential

The methodology proposed in this study provides a suitable workflow for mapping alpine peatlands, despite its tendency to overestimate the peatland areas. Our approach identified a total area of 11.635 km^2 peatlands, whereas the inventory provided by public administrations reports an area of 7.764 km^2 (see Section 2.2). This clearly indicates an overestimation by the applied methodology. However, it is worth noting that the reliability of the Natura 2000 database—on which the inventory is largely based—may be limited. Previous studies Opermanis et al. (2012) and Blondet et al. (2017) have highlighted that peatland coverage in Natura 2000 is potentially underestimated due to inconsistent survey efforts, outdated records, and varying detection methods among countries. Given that the database used in this study is largely derived from Natura 2000, this may have contributed to the observed discrepancy. That said, we acknowledge that the overestimation produced by our method is too large to be attributed solely to shortcomings in the inventory and thus warrants further investigation.

Three other factors mainly related to remote sensing could be sources for the overestimation in our results. The variability of plant species and height within peatlands poses a challenge for peatland identification from remote sensing images, as it increases the heterogeneity of information provided to the RF algorithm. Detailed information on plant species that were not available for this study could potentially provide a better data set to reduce spatial heterogeneity within a site, thereby improving RF performance and reducing overestimation. The second is the band and resolution limit of current employed microwave and optical remote sensing imagery. The third factor is the lack of high-resolution soil maps, such as detailed maps of soil organic content, which could greatly improve classification accuracy and help eliminate FPs and reduce overestimations. The upcoming NASA-ISRO (NISAR) SAR mission (Kellogg et al., 2020), with longer wavelength S-band and L-band, will probably help in reducing overestimation issues (Huang et al., 2017). The high 3 m resolution Planet data (Planet Labs PBC, 2024) is probably one of the solutions to accurately detect small alpine peatlands. The application of other remote sensing methods based on electromagnetic induction data (Boaga et al., 2020; Silvestri, Christensen, et al., 2019; Silvestri, Knight, et al., 2019) are also extremely promising, especially to explore large valleys with a high presence of peatland sites.

5. Conclusions

With the increasing impact of global anthropogenic activities and climate change, enhancing our understanding of alpine peatlands has become an essential aspect of environmental management. The study presents an effective, efficient and low-cost approach based on a pixel-based RF algorithm for mapping alpine peatlands. To the best of our knowledge, this is the first attempt to map the Italian Alpine peatlands using time series of Sentinel-1 and Sentinel-2 data and DEM on GEE platform. Our approach detects peatlands covering a total area of 11.635 km^2 in the Avisio basin. The accuracy reaches 99%, 90.5% and 0.8% of PPV, OA and FPs, respectively. DEM derived and topographic variables are more important to alpine peatland mapping than hydrological, optical and microwave variables.

Despite the strong performance of the method, the area of Alpine peatlands appears to be misclassified due to their small extent, complex topography, and the similar ground characteristics of peatlands and vegetated lands captured and interpreted by optical and microwave remote sensing imagery. Reducing this misclassification remains a challenge for accurately mapping Alpine peatlands in future research.

Data Availability Statement

The GLO-30 data set (European Space Agency, 2024) that supports the findings of this study is openly available in Copernicus Data Space Ecosystem at https://doi.org/10.5270/ESA-c5d3d65. The LiDAR DTM data that support the findings of this study is published on the Trentino Cartographic Geoportal can be findable and accessible at https://siat.provincia.tn.it/stem/. 3.22.13 of QGIS (QGIS.org, 2022) and 7.8.2 SAGA GIS (Conrad et al., 2015) used for processing satellite imageries is preserved at https://www.qgis.org/ and https://sourceforge.net/projects/saga-gis/files/, available via free access. Furthermore, the 165 peatland sites data set and the GEE code supporting the study can be accessed from the Zenodo (Q. Li et al., 2024b).

Acknowledgments
The authors gratefully acknowledge financial support from China Scholarship Council. This work was partially carried out as part of the project "CHANGED—CHAracteriziNG pEatlands from Drones," funded by the University of Padua (Italy) by means of the STARS Consolidator Grants. MS was at the University of Potsdam as Alexander von Humboldt Postdoctoral Fellow during the research phase of the manuscript and presently at Aberystwyth University as Royal Society—Newton International Fellow and gratefully acknowledges these universities and the funding agencies the Alexander von Humboldt Foundation, Germany and the Royal Society, UK. This study was partially carried out within the RETURN Extended Partnership and received funding from the European Union Next-GenerationEU (National Recovery and Resilience Plan—NRRP, Mission 4, Component 2, Investment 1.3—D.D. 1243 2/8/2022, PE0000005). Open access publishing facilitated by Universita degli Studi di Bologna, as part of the Wiley - CRUI-CARE agreement.

References

Amani, M., Salehi, B., Mahdavi, S., & Brisco, B. (2019). Separability analysis of wetlands in Canada using multi-source SAR data. *GIScience and Remote Sensing*, *56*(8), 1233–1260. https://doi.org/10.1080/15481603.2019.1643530

Amani, M., Salehi, B., Mahdavi, S., Granger, J. E., Brisco, B., & Hanson, A. (2017). Wetland classification using multi-source and multi-temporal optical remote sensing data in Newfoundland and Labrador, Canada. *Canadian Journal of Remote Sensing*, *43*(4), 360–373. https://doi.org/10.1080/07038992.2017.1346468

Anaya, J. A., Colditz, R. R., & Valencia, G. M. (2015). Land cover mapping of a tropical region by integrating multi-year data into an annual time series. *Remote Sensing*, *7*(12), 16274–16292. https://doi.org/10.3390/rs71215833

Assiri, M., Sartori, A., Persichetti, A., Miele, C., Faelga, R. A., Blount, T., & Silvestri, S. (2023). Leaf area index and aboveground biomass estimation of an alpine peatland with a UAV multi-sensor approach. *GIScience and Remote Sensing*, *60*(1), 2270791. https://doi.org/10.1080/15481603.2023.2270791

Balsiger, J. (2016). The European Union strategy for the Alpine region. In *A "macro-regional" Europe in the making: Theoretical approaches empirical evidence* (pp. 189–213). https://doi.org/10.1080/00343404.2016.1217406

Bechtel, T. D., & Goldscheider, N. (2017). Geoelectrical fingerprinting of two contrasting ecohydrological peatland types in the Alps. *Wetlands*, *37*(5), 875–884. https://doi.org/10.1007/s13157-017-0921-5

Belgiu, M., & Drăguţ, L. (2016). Random forest in remote sensing: A review of applications and future directions. *ISPRS Journal of Photogrammetry and Remote Sensing*, *114*, 24–31. https://doi.org/10.1016/j.isprsjprs.2016.01.011

Blondet, M., de Koning, J., Borrass, L., Ferranti, F., Geitzenauer, M., Weiss, G., et al. (2017). Participation in the implementation of Natura 2000: A comparative study of six EU member states. *Land Use Policy*, *66*, 346–355. https://doi.org/10.1016/j.landusepol.2017.04.004

Boaga, J., Viezzoli, A., Cassiani, G., Deidda, G., Tosi, L., & Silvestri, S. (2020). Resolving the thickness of peat deposits with contact-less electromagnetic methods: A case study in the Venice coastland. *Science of the Total Environment*, *737*, 139361. https://doi.org/10.1016/j.scitotenv.2020.139361

Böhner, J., & Selige, T. (2006). Spatial prediction of soil attributes using terrain analysis and climate regionalisation. In *SAGA-analyses and modelling applications: Goltze*.

Breiman, L. (2001). Random forests. *Machine Learning*, *45*(1), 5–32. https://doi.org/10.1023/a:1010933404324

Brown, C., Boyd, D. S., Sjögersten, S., & Vane, C. H. (2023). Detecting tropical peatland degradation: Combining remote sensing and organic geochemistry. *PLoS One*, *18*(3), e0280187. https://doi.org/10.1371/journal.pone.0280187

Camill, P. (2005). Permafrost thaw accelerates in boreal peatlands during late-20th century climate warming. *Climatic Change*, *68*(1–2), 135–152. https://doi.org/10.1007/s10584-005-4785-y

Carbognani, M., Tomaselli, M., & Petraglia, A. (2023). Interactions and covariation of ecological drivers control CO_2 fluxes in an Alpine Peatland. *Wetlands*, *43*(5), 1–16. https://doi.org/10.1007/s13157-023-01692-5

Cavalli, M., Trevisani, S., Comiti, F., & Marchi, L. (2013). Geomorphometric assessment of spatial sediment connectivity in small Alpine catchments. *Geomorphology*, *188*, 31–41. https://doi.org/10.1016/j.geomorph.2012.05.007

Chen, H., Yang, G., Peng, C., Zhang, Y., Zhu, D., Zhu, Q., et al. (2014). The carbon stock of alpine peatlands on the Qinghai–Tibetan Plateau during the Holocene and their future fate. *Quaternary Science Reviews*, *95*, 151–158. https://doi.org/10.1016/j.quascirev.2014.05.003

Chen, Z., Ye, F., Fu, W., Ke, Y., & Hong, H. (2020). The influence of DEM spatial resolution on landslide susceptibility mapping in the Baxie River basin, NW China. *Natural Hazards*, *101*(3), 853–877. https://doi.org/10.1007/s11069-020-03899-9

Chimner, R. A., Bourgeau-Chavez, L., Grelik, S., Hribljan, J. A., Clarke, A. M. P., Polk, M. H., et al. (2019). Mapping mountain peatlands and wet meadows using multi-date, multi-sensor remote sensing in the Cordillera Blanca, Peru. *Wetlands*, *39*(5), 1057–1067. https://doi.org/10.1007/s13157-019-01134-1

Cohen, J. (1960). A coefficient of agreement for nominal scales. *Educational and Psychological Measurement*, *20*(1), 37–46. https://doi.org/10.1177/001316446002000104

Conrad, O., Bechtel, B., Bock, M., Dietrich, H., Fischer, E., Gerlitz, L., et al. (2015). System for automated geoscientific analyses (SAGA) v. 2.1.4. *Geoscientific Model Development*, *8*(7), 1991–2007. https://doi.org/10.5194/gmd-8-1991-2015

Cremonini, S., Etiope, G., Italiano, F., & Martinelli, G. (2008). Evidence of possible enhanced peat burning by deep-origin methane in the Po River Delta Plain (Italy). *The Journal of Geology*, *116*(4), 401–413. https://doi.org/10.1086/588835

Crespi, A., Matiu, M., Bertoldi, G., Petitta, M., & Zebisch, M. (2021). A high-resolution gridded dataset of daily temperature and precipitation records (1980–2018) for Trentino-South Tyrol (north-eastern Italian Alps). *Earth System Science Data*, *13*(6), 2801–2818. https://doi.org/10.5194/essd-13-2801-2021

Dai, W., Yang, X., Na, J., Li, J., Brus, D., Xiong, L., et al. (2019). Effects of DEM resolution on the accuracy of gully maps in loess hilly areas. *Catena*, *177*, 114–125. https://doi.org/10.1016/j.catena.2019.02.010

Dalponte, M., Ørka, H. O., Gobakken, T., Gianelle, D., & Næsset, E. (2012). Tree species classification in boreal forests with hyperspectral data. *IEEE Transactions on Geoscience and Remote Sensing*, *51*(5), 2632–2645. https://doi.org/10.1109/TGRS.2012.2216272

DeLancey, E. R., Kariyeva, J., Bried, J. T., & Hird, J. N. (2019). Large-scale probabilistic identification of boreal peatlands using Google Earth Engine, open-access satellite data, and machine learning. *PLoS One*, *14*(6), e0218165. https://doi.org/10.1371/journal.pone.0218165

Dessalegn, D., Beyene, S., Ram, N., Walley, F., & Gala, T. S. (2014). Effects of topography and land use on soil characteristics along the toposequence of Ele watershed in southern Ethiopia. *Catena*, *115*, 47–54. https://doi.org/10.1016/j.catena.2013.11.007

DEWHA. (2009). *Alpine sphagnum bogs and associated fens: A nationally threatened ecological community. EPBC Act 1999 Policy Statement 3.16*. Commonwealth of Australia. Retrieved from https://www.agriculture.gov.au/sites/default/files/documents/alpine-sphagnum-bogs.pdf

Du, P., Samat, A., Waske, B., Liu, S., & Li, Z. (2015). Random forest and rotation forest for fully polarized SAR image classification using polarimetric and spatial features. *ISPRS Journal of Photogrammetry and Remote Sensing*, *105*, 38–53. https://doi.org/10.1016/j.isprsjprs.2015.03.002

European Space Agency. (2024). Copernicus global digital elevation model. https://doi.org/10.5270/ESA-c5d3d65

European Commission, Environment, D.-G. F., Mézard, N., Sundseth, K., & Wegefelt, S. (2008). In N. Mézard (Ed.), *Natura 2000—Protecting Europe's biodiversity*. European Commission. Retrieved from https://data.europa.eu/doi/10.2779/45963

Fischer, G., Nachtergaele, F., Prieler, S., Velthuizen, H. T. V., & Verelst, L. (2008). *Global Agro-ecological Zones Assessment for Agriculture (GAEZ 2008)*. IIASA. Retrieved from https://www.gaez.iiasa.ac.at/docs/GAEZ_Model_Documentation.pdf

Frolking, S., Talbot, J., Jones, M. C., Treat, C. C., Kauffman, J. B., Tuittila, E.-S., & Roulet, N. (2011). Peatlands in the Earth's 21st century climate system. *Environmental Reviews*, *19*(NA), 371–396. https://doi.org/10.1139/a11-014

Gallego, F. J. (2004). Remote sensing and land cover area estimation. *International Journal of Remote Sensing*, *25*(15), 3019–3047. https://doi.org/10.1080/01431160310001619607

Gao, B. (1996). NDWI—A normalized difference water index for remote sensing of vegetation liquid water from space. *Remote Sensing of Environment*, *58*(3), 257–266. https://doi.org/10.1016/S0034-4257(96)00067-3

Garroway, K., Hopkinson, C., & Jamieson, R. (2011). Surface moisture and vegetation influences on lidar intensity data in an agricultural watershed. *Canadian Journal of Remote Sensing*, *37*(3), 275–284. https://doi.org/10.5589/m11-036

Gerdol, R., Tomaselli, M., & Bragazza, L. (1994). A floristic-ecologic classification of five mire sites in the montane-subalpine belt of South Tyrol (S Alps, Italy).

Ghimire, B., Rogan, J., Galiano, V. R., Panday, P., & Neeti, N. (2012). An evaluation of bagging, boosting, and random forests for land-cover classification in Cape Cod, Massachusetts, USA. *GIScience and Remote Sensing*, *49*(5), 623–643. https://doi.org/10.2747/1548-1603.49.5.623

Gorelick, N., Hancher, M., Dixon, M., Ilyushchenko, S., Thau, D., & Moore, R. (2017). Google Earth Engine: Planetary-scale geospatial analysis for everyone. *Remote Sensing of Environment*, *202*, 18–27. https://doi.org/10.1016/j.rse.2017.06.031

Grzybowski, M., & Glińska-Lewczuk, K. (2020). The principal threats to the peatlands habitats, in the continental bioregion of Central Europe–A case study of peatland conservation in Poland. *Journal for Nature Conservation*, *53*, 125778. https://doi.org/10.1016/j.jnc.2019.125778

Gumbricht, T., Roman-Cuesta, R. M., Verchot, L., Herold, M., Wittmann, F., Householder, E., et al. (2017). An expert system model for mapping tropical wetlands and peatlands reveals South America as the largest contributor. *Global Change Biology*, *23*(9), 3581–3599. https://doi.org/10.1111/gcb.13689

Hall, D. K., Riggs, G. A., & Salomonson, V. V. (1995). Development of methods for mapping global snow cover using moderate resolution imaging spectroradiometer data. *Remote Sensing of Environment*, *54*(2), 127–140. https://doi.org/10.1016/0034-4257(95)00137-P

Hendriks, D., Van Huissteden, J., Dolman, A., & Van der Molen, M. (2007). The full greenhouse gas balance of an abandoned peat meadow. *Biogeosciences*, *4*(3), 411–424. https://doi.org/10.5194/bg-4-411-2007

Hengl, T., Mendes de Jesus, J., Heuvelink, G. B., Ruiperez Gonzalez, M., Kilibarda, M., Blagotić, A., et al. (2017). SoilGrids250m: Global gridded soil information based on machine learning. *PLoS One*, *12*(2), e0169748. https://doi.org/10.1371/journal.pone.0169748

Hribljan, J. A., Hough, M., Lilleskov, E. A., Suarez, E., Heckman, K., Planas-Clarke, A. M., & Chimner, R. A. (2024). Elevation and temperature are strong predictors of long-term carbon accumulation across tropical Andean mountain peatlands. *Mitigation and Adaptation Strategies for Global Change*, *29*(1), 1. https://doi.org/10.1007/s11027-023-10089-y

Hribljan, J. A., Suarez, E., Bourgeau-Chavez, L., Endres, S., Lilleskov, E. A., Chimbolema, S., et al. (2017). Multidate, multisensor remote sensing reveals high density of carbon-rich mountain peatlands in the páramo of Ecuador. *Global Change Biology*, *23*(12), 5412–5425. https://doi.org/10.1111/gcb.13807

Huang, Y., Levy-Vehel, J., Ferro-Famil, L., & Reigber, A. (2017). Three-dimensional imaging of objects concealed below a forest canopy using SAR tomography at L-band and wavelet-based sparse estimation. *IEEE Geoscience Remote Sensing Letters*, *14*(9), 1454–1458. https://doi.org/10.1109/LGRS.2017.2709839

Huete, A., Didan, K., Miura, T., Rodriguez, E. P., Gao, X., & Ferreira, L. G. (2002). Overview of the radiometric and biophysical performance of the MODIS vegetation indices. *Remote Sensing of Environment*, *83*(1–2), 195–213. https://doi.org/10.1016/S0034-4257(02)00096-2

Iwahashi, J., & Pike, R. J. (2007). Automated classifications of topography from DEMs by an unsupervised nested-means algorithm and a three-part geometric signature. *Geomorphology*, *86*(3–4), 409–440. https://doi.org/10.1016/j.geomorph.2006.09.012

Izquierdo, A. E., Foguet, J., & Ricardo Grau, H. (2015). Mapping and spatial characterization of Argentine High Andean peatbogs. *Wetlands Ecology and Management*, *23*(5), 963–976. https://doi.org/10.1007/s11273-015-9433-3

Jin, H., Stehman, S. V., & Mountrakis, G. (2014). Assessing the impact of training sample selection on accuracy of an urban classification: A case study in Denver, Colorado. *International Journal of Remote Sensing*, *35*(6), 2067–2081. https://doi.org/10.1080/01431161.2014.885152

Kariminejad, N., Hosseinalizadeh, M., Pourghasemi, H. R., Ownegh, M., Rossi, M., & Tiefenbacher, J. P. (2020). Optimizing collapsed pipes mapping: Effects of DEM spatial resolution. *Catena*, *187*, 104344. https://doi.org/10.1016/j.catena.2019.104344

Kellogg, K., Hoffman, P., Standley, S., Shaffer, S., Rosen, P., Edelstein, W., et al. (2020). NASA-ISRO synthetic aperture radar (NISAR) mission. In *Paper presented at the 2020 IEEE Aerospace Conference*. https://doi.org/10.1109/AERO47225.2020.9172638

Khan, A., Said, A., & Ullah, I. (2020). Landsat based distribution mapping of high-altitude peatlands in Hindu Kush Himalayas—A case study of Broghil Valley, Pakistan. *Journal of Mountain Science*, *17*(1), 42–49. https://doi.org/10.1007/s11629-019-5384-0

Kinnell, P. I. (2005). Alternative approaches for determining the USLE-M slope length factor for grid cells. *Soil Science Society of America Journal*, *69*(3), 674–680. https://doi.org/10.2136/sssaj2004.0047

Lee, W., & Seo, K. (2022). Downsampling for binary classification with a highly imbalanced dataset using active learning. *Big Data Research*, *28*, 100314. https://doi.org/10.1016/j.bdr.2022.100314

Li, A., Song, K., Chen, S., Mu, Y., Xu, Z., & Zeng, Q. (2022). Mapping African wetlands for 2020 using multiple spectral, geo-ecological features and Google Earth Engine. *Journal of photogrammetry remote sensing*, *193*, 252–268. https://doi.org/10.1016/j.isprsjprs.2022.09.009

Li, Q., Liu, G., & Chen, W. (2021). Toward a simple and generic approach for identifying multi-year cotton cropping patterns using Landsat and Sentinel-2 time series. *Remote Sensing*, *13*(24), 5183. https://doi.org/10.3390/rs13245183

Li, Q., Singh, M., & Silvestri, S. (2024a). Mapping Italian Alpine Peatlands using multisource satellite imagery and machine learning approach. https://doi.org/10.5194/egusphere-egu24-13540

Li, Q., Singh, M., & Silvestri, S. (2024b). Remote sensing of Alpine Peatlands: Challenges of mapping thousands of sparse small sites scattered across extensive mountainous territories [Dataset]. *Zenodo*. https://doi.org/10.5281/zenodo.14318391

Maiorano, L., Falcucci, A., Garton, E. O., & Boitani, L. (2007). Contribution of the Natura 2000 network to biodiversity conservation in Italy. *Conservation Biology*, *21*(6), 1433–1444. https://doi.org/10.1111/j.1523-1739.2007.00831.x

Manfreda, S., & Fiorentino, M. (2008). Flood volume estimation and flood mitigation: Adige River Basin. In *Mountains: Sources of Water, Sources of Knowledge* (pp. 243–264). https://doi.org/10.1007/978-1-4020-6748-8_15

Martinelli, G., Cremonini, S., & Samonati, E. (2012). The peat fires of Italy. In *Coal & peat fires: A global perspective, 2-Photographs and Multimedia Tours* (pp. 205–216). Elsevier. https://doi.org/10.1016/B978-0-444-59510-2.00003-3

Martini, L., Baggio, T., Torresani, L., Crema, S., & Cavalli, M. (2022). R_IC: A novel and versatile implementation of the index of connectivity in R. *Environmental Modelling & Software*, *155*, 105446. https://doi.org/10.1016/j.envsoft.2022.105446

Melton, J. R., Chan, E., Millard, K., Fortier, M., Winton, R. S., Martín-López, J. M., et al. (2022). A map of global peatland extent created using machine learning (Peat-ML). *Geoscientific Model Development*, *15*(12), 4709–4738. https://doi.org/10.5194/gmd-15-4709-2022

Menze, B. H., Kelm, B. M., Masuch, R., Himmelreich, U., Bachert, P., Petrich, W., & Hamprecht, F. A. (2009). A comparison of random forest and its Gini importance with standard chemometric methods for the feature selection and classification of spectral data. *BMC Bioinformatics*, *10*, 1–16. https://doi.org/10.1186/1471-2105-10-213

Millard, K. (2016). *Development of methods to map and monitor peatland ecosystems and hydrologic conditions using Radarsat-2 Synthetic Aperture Radar*. Carleton University.

Millard, K., & Richardson, M. (2013). Wetland mapping with LiDAR derivatives, SAR polarimetric decompositions, and LiDAR–SAR fusion using a random forest classifier. *Canadian Journal of Remote Sensing*, *39*(4), 290–307. https://doi.org/10.5589/m13-038

Miller, M. P., Singer, M. J., & Nielsen, D. R. (1988). Spatial variability of wheat yield and soil properties on complex hills. *Soil Science Society of America Journal*, *52*(4), 1133–1141. https://doi.org/10.2136/sssaj1988.03615995005200040045x

Minasny, B., Adetsu, D. V., Aitkenhead, M., Artz, R. R., Baggaley, N., Barthelmes, A., et al. (2024). Mapping and monitoring peatland conditions from global to field scale. *Biogeochemistry*, *167*(4), 383–425. https://doi.org/10.1007/s10533-023-01084-1

Minasny, B., Berglund, Ö., Connolly, J., Hedley, C., de Vries, F., Gimona, A., et al. (2019). Digital mapping of peatlands–A critical review. *Earth-Science Reviews*, *196*, 102870. https://doi.org/10.1016/j.earscirev.2019.05.014

Nugent, K. A., Strachan, I. B., Strack, M., Roulet, N. T., & Rochefort, L. (2018). Multi-year net ecosystem carbon balance of a restored peatland reveals a return to carbon sink. *Global Change Biology*, *24*(12), 5751–5768. https://doi.org/10.1111/gcb.14449

Olaya, V., & Conrad, O. (2009). Geomorphometry in SAGA. *Developments in Soil Science*, *33*, 293–308. https://doi.org/10.1016/S0166-2481(08)00012-3

O'Neill, H., Burn, C., Allard, M., Arenson, L., Bunn, M., Connon, R., et al. (2020). Permafrost thaw and northern development. *Nature Climate Change*, *10*(8), 722–723. https://doi.org/10.1038/s41558-019-0614-6

Onojeghuo, A. O., Onojeghuo, A. R., Cotton, M., Potter, J., & Jones, B. (2021). Wetland mapping with multi-temporal sentinel-1 &-2 imagery (2017–2020) and LiDAR data in the grassland natural region of Alberta. *GIScience and Remote Sensing*, *58*(7), 999–1021. https://doi.org/10.1080/15481603.2021.1952541

Opermanis, O., MacSharry, B., Aunins, A., & Sipkova, Z. (2012). Connectedness and connectivity of the Natura 2000 network of protected areas across country borders in the European Union. *Biological Conservation*, *153*, 227–238. https://doi.org/10.1016/j.biocon.2012.04.031
Parish, F., Sirin, A., Charman, D., Joosten, H., Minaeva, T. Y., & Silvius, M. (2008). Assessment on peatlands, biodiversity and climate change.
Patthey, P., Wirthner, S., Signorell, N., & Arlettaz, R. (2008). Impact of outdoor winter sports on the abundance of a key indicator species of alpine ecosystems. *Journal of Applied Ecology*, *45*(6), 1704–1711. https://doi.org/10.1111/j.1365-2664.2008.01547.x
Planet Labs, P. B. C. (2024). Planet Application Program interface: In space for life on Earth [Dataset]. *Planets*. https://api.planet.com
Poto, L., Gabrieli, J., Crowhurst, S. J., Appleby, P. G., Ferretti, P., Surian, N., et al. (2013). The first continuous Late Glacial–Holocene peat bog multi-proxy record from the Dolomites (NE Italian Alps). *Quaternary International*, *306*, 71–79. https://doi.org/10.1016/j.quaint.2013.05.001
Pullens, J., Sottocornola, M., Kiely, G., Toscano, P., & Gianelle, D. (2016). Carbon fluxes of an alpine peatland in Northern Italy. *Agricultural and Forest Meteorology*, *220*, 69–82. https://doi.org/10.1016/j.agrformet.2016.01.012
QGIS.org. (2022). *QGIS 3.22. QGIS geographic information system*. QGIS Association. Retrieved from https://www.qgis.org
Räsänen, A., Aurela, M., Juutinen, S., Kumpula, T., Lohila, A., Penttilä, T., & Virtanen, T. (2020). Detecting northern peatland vegetation patterns at ultra-high spatial resolution. *Remote Sensing in Ecology Conservation biology*, *6*(4), 457–471. https://doi.org/10.1002/rse2.140
Räsänen, A., & Virtanen, T. (2019). Data and resolution requirements in mapping vegetation in spatially heterogeneous landscapes. *Remote Sensing of Environment*, *230*, 111207. https://doi.org/10.1016/j.rse.2019.05.026
Reichart, F. A. F. (2020). *Data availability of the peatlands in the Alps: Investigation of the current status, deficit-analysis and concepts for peatland corridors, (master dissertation)*. Technischen Universität München.
Ribeiro, K., Pacheco, F. S., Ferreira, J. W., de Sousa-Neto, E. R., Hastie, A., Krieger Filho, G. C., et al. (2021). Tropical peatlands and their contribution to the global carbon cycle and climate change. *Global Change Biology*, *27*(3), 489–505. https://doi.org/10.1111/gcb.15408
Rodriguez-Galiano, V. F., Ghimire, B., Rogan, J., Chica-Olmo, M., & Rigol-Sanchez, J. P. (2012). An assessment of the effectiveness of a random forest classifier for land-cover classification. *ISPRS Journal of Photogrammetry and Remote Sensing*, *67*, 93–104. https://doi.org/10.1016/j.isprsjprs.2011.11.002
Rouse, J. W., Jr., Haas, R. H., Deering, D., Schell, J., & Harlan, J. C. (1974). Monitoring the vernal advancement and retrogradation (green wave effect) of natural vegetation. Retrieved from https://ntrs.nasa.gov/api/citations/19750020419/downloads/19750020419.pdf
Rowland, J. A., Moore, J. L., & Walsh, J. C. (2023). How expert insight into alpine peatland conservation complements global scientific evidence. *Conservation Biology*, *37*(3), e14081. https://doi.org/10.1111/cobi.14081
Runfola, D., Anderson, A., Baier, H., Crittenden, M., Dowker, E., Fuhrig, S., et al. (2020). geoBoundaries: A global database of political administrative boundaries. *PLoS One*, *15*(4), e0231866. https://doi.org/10.1371/journal.pone.0231866
Sadeghi, M., Babaeian, E., Tuller, M., & Jones, S. B. (2017). The optical trapezoid model: A novel approach to remote sensing of soil moisture applied to Sentinel-2 and Landsat-8 observations. *Remote Sensing of Environment*, *198*, 52–68. https://doi.org/10.1016/j.rse.2017.05.041
Samuele, D. P., Filippo, S., Orusa, T., & Enrico, B.-M. (2021). Mapping SAR geometric distortions and their stability along time: A new tool in Google Earth Engine based on Sentinel-1 image time series. *International Journal of Remote Sensing*, *42*(23), 9135–9154. https://doi.org/10.1080/01431161.2021.1992035
Silvestri, S., Christensen, C. W., Lysdahl, A. O., Anschütz, H., Pfaffhuber, A. A., & Viezzoli, A. (2019). Peatland volume mapping over resistive substrates with airborne electromagnetic technology. *Geophysical Research Letters*, *46*(12), 6459–6468. https://doi.org/10.1029/2019GL083025
Silvestri, S., Knight, R., Viezzoli, A., Richardson, C. J., Anshari, G. Z., Dewar, N., et al. (2019). Quantification of peat thickness and stored carbon at the landscape scale in tropical peatlands: A comparison of airborne geophysics and an empirical topographic method. *Journal of Geophysical Research: Earth Surface*, *124*(12), 3107–3123. https://doi.org/10.1029/2019JF005273
Singh, M., & Sinha, R. (2022). Integrating hydrological connectivity in a process–response framework for restoration and monitoring prioritisation of floodplain wetlands in the Ramganga Basin, India. *Water*, *14*(21), 3520. https://doi.org/10.3390/w14213520
Singh, M., Sinha, R., Mishra, A., & Babu, S. (2022). Wetlandscape (dis) connectivity and fragmentation in a large wetland (Haiderpur) in west Ganga plains, India. *Earth Surface Processes and Landforms*, *47*(7), 1872–1887. https://doi.org/10.1002/esp.5352
Steenvoorden, J., & Limpens, J. (2023). Upscaling peatland mapping with drone-derived imagery: Impact of spatial resolution and vegetation characteristics. *GIScience and Remote Sensing*, *60*(1), 2267851. https://doi.org/10.1080/15481603.2023.2267851
Strack, M., Hayne, S., Lovitt, J., McDermid, G. J., Rahman, M. M., Saraswati, S., & Xu, B. (2019). Petroleum exploration increases methane emissions from northern peatlands. *Nature Communications*, *10*(1), 2804. https://doi.org/10.1038/s41467-019-10762-4
Sun, J., Gallego-Sala, A., & Yu, Z. (2023). Topographic and climatic controls of peatland distribution on the Tibetan Plateau. *Scientific Reports*, *13*(1), 14811. https://doi.org/10.1038/s41598-023-39699-x
Sun, X., Yin, D., Qin, F., Yu, H., Lu, W., Yao, F., et al. (2023). Revealing influencing factors on global waste distribution via deep-learning based dumpsite detection from satellite imagery. *Nature Communications*, *14*(1), 1444. https://doi.org/10.1038/s41467-023-37136-1
Tanneberger, F., & Belous, T. (2017). The peatland map of Europe. *Mires & Peat*, (19). https://doi.org/10.19189/MaP.2016.OMB.264
Tao, M., Lai, S., Li, J., Su, J., Fan, Y., & Wang, L. (2021). Extraction and mitigation of radio frequency interference artifacts based on time-series Sentinel-1 SAR data. *IEEE Transactions on Geoscience and Remote Sensing*, *60*, 1–11. https://doi.org/10.1109/TGRS.2021.3126485
Torres, R., Snoeij, P., Geudtner, D., Bibby, D., Davidson, M., Attema, E., et al. (2012). GMES Sentinel-1 mission. *Remote Sensing of Environment*, *120*, 9–24. https://doi.org/10.1016/j.rse.2011.05.028
Turetsky, M. R., Abbott, B. W., Jones, M. C., Anthony, K. W., Olefeldt, D., Schuur, E. A., et al. (2020). Carbon release through abrupt permafrost thaw. *Nature Geoscience*, *13*(2), 138–143. https://doi.org/10.1038/s41561-019-0526-0
Uemoto, J., Nadai, A., Kojima, S., Kobayashi, T., Umehara, T., Matsuoka, T., et al. (2018). Extraction and height estimation of artificial vertical structures based on the wrapped interferometric phase difference within their layovers. *ISPRS Journal of Photogrammetry and Remote Sensing*, *139*, 14–29. https://doi.org/10.1016/j.isprsjprs.2018.02.018
UNEP. (2022). Global peatlands assessment–the state of the world's peatlands: Evidence for action toward the conservation, restoration, and sustainable management of peatlands. Retrieved from https://www.unep.org/resources/global-peatlands-assessment-2022
Valois, R., Schaffer, N., Figueroa, R., Maldonado, A., Yáñez, E., Hevia, A., et al. (2020). Characterizing the water storage capacity and hydrological role of mountain peatlands in the arid Andes of north-central Chile. *Water*, *12*(4), 1071. https://doi.org/10.3390/w12041071
van der Velde, Y., Temme, A. J., Nijp, J. J., Braakhekke, M. C., van Voorn, G. A., Dekker, S. C., et al. (2021). Emerging forest–peatland bistability and resilience of European peatland carbon stores. *Proceedings of the National Academy of Sciences of the United States of America*, *118*(38), e2101742118. https://doi.org/10.1073/pnas.2101742118
Vitt, D. H., Halsey, L. A., Bauer, I. E., & Campbell, C. (2000). Spatial and temporal trends in carbon storage of peatlands of continental western Canada through the Holocene. *Canadian Journal of Earth Sciences*, *37*(5), 683–693. https://doi.org/10.1139/e99-097
Wan, T., Jun, H., Zhang, H., Pan, W., & Hua, H. (2015). Kappa coefficient: A popular measure of rater agreement. *Shanghai archives of psychiatry*, *27*(1), 62–67. https://doi.org/10.11919/j.issn.1002-0829.215010

Wang, J., Fu, B., Qiu, Y., & Chen, L. (2001). Soil nutrients in relation to land use and landscape position in the semi-arid small catchment on the Loess plateau in China. *Journal of Arid Environments*, *48*(4), 537–550. https://doi.org/10.1006/jare.2000.0763

Witze, A. (2020). Why Arctic fires are bad news for climate change. *Nature*, *585*(7825), 336–337. https://doi.org/10.1038/d41586-020-02568-y

Wood, J. (1996). *The geomorphological characterisation of digital elevation models*. University of Leicester.

Wood, J. (2009). Geomorphometry in landserf. *Developments in Soil Science*, *33*, 333–349. https://doi.org/10.1016/S0166-2481(08)00014-7

Wu, Y., Chan, E., Melton, J. R., & Verseghy, D. L. (2017). A map of global peatland distribution created using machine learning for use in terrestrial ecosystem and Earth system models. *Geoscientific Model Development Discussions*, 1–21. https://doi.org/10.5194/gmd-2017-152

Xu, J., Morris, P. J., Liu, J., & Holden, J. (2018). PEATMAP: Refining estimates of global peatland distribution based on a meta-analysis. *Catena*, *160*, 134–140. https://doi.org/10.1016/j.catena.2017.09.010

Zeng, X., Hu, Z., Chen, A., Yuan, W., Hou, G., Han, D., et al. (2022). The global decline in the sensitivity of vegetation productivity to precipitation from 2001 to 2018. *Global Change Biology*, *28*(22), 6823–6833. https://doi.org/10.1111/gcb.16403

Zeyliger, A., Muzalevskiy, K., Zinchenko, E., & Ermolaeva, O. J. S. O. T. T. E. (2022). Field test of the surface soil moisture mapping using Sentinel-1 radar data. *Science of the Total Environment*, *807*, 151121. https://doi.org/10.1016/j.scitotenv.2021.151121

Zilioli, D. M., Bini, C., Wahsha, M., & Ciotoli, G. J. G. (2011). The pedological heritage of the Dolomites (Northern Italy): Features, distribution and evolution of the soils, with some implications for land management. *Geomorphology*, *135*(3–4), 232–247. https://doi.org/10.1016/j.geomorph.2011.02.004